Growth of zirconia and yttria-stabilized zirconia nanorod arrays assisted by phase transition

Chih-Chiang Chen,[a] Wei-Yun Cheng,[a] Shih-Yuan Lu,*[a] Yi-Feng Lin,*[b] Yung-Jung Hsu,[c] Kai-Shiun Chang,[b] Chao-Hsiang Kang[b] and Kuo-Lun Tung[b]

Well-aligned, densely distributed ZrO_2 nanorod arrays were fabricated using a non-catalytic, template-free metal–organic chemical vapour deposition process at a reaction temperature of 1000 °C. The reaction temperature was found to play a key role in product morphology, with particle thin films obtained at 550 °C and nanorod arrays produced at 1000 °C. Increasing the reaction temperature led to the emergence of the medium-temperature tetragonal phase from the dominant low-temperature monoclinic phase, which is advantageous for anisotropic growth necessary for the nanorod formation. With the same deposition process, yttria-stabilized zirconia nanorod arrays of polycrystalline cubic phase were fabricated by co-feeding the dopant precursor, YCl_3, with the zirconia precursor, $Zr(C_5H_7O_2)_4$. The present work demonstrated the first example of monoclinic to tetragonal phase-transition assisted one-dimensional (1D) growth, and the concept can be extended to the formation of 1D nanostructures of materials possessing the monoclinic-tetragonal polymorphism.

Introduction

Well-aligned, one-dimensional (1D) nanostructures such as nanorod and nanowire arrays have attracted a great deal of research attention in recent years because of their wide range applications in nanodevices, such as field emitters,[1] sensors,[2] piezoelectric nanogenerators,[3,4] etc. A wide variety of technologically important 1D arrays, including CdS,[5] ZnO,[6] Ag,[7] GaN,[8] ZnTe,[9] and Sb_2Te_3,[10] has been successfully fabricated by using anodic aluminium oxide (AAO) membranes as the sacrificial template or through the vapour–liquid–solid (VLS) growth mechanism. These processes, however, involve usage of sacrificial templates or guiding catalysts, whose removal may complicate the applications of these arrays. An advantageous way for fabrication of 1D nanoarrays is via non-catalytic, template-free processes to avoid the potential post-reaction removal of the involved templates or catalysts.

Previously, we have successfully prepared plain CdS[1] as well as coaxial CdS–CdO and ZnS–ZnO[11] nanorod arrays using non-catalytic, template-free metal organic chemical vapour deposition (MOCVD) processes. Zirconia and yttria-stabilized zirconia (YSZ) have vital applications in sensors,[12] solid oxide electrolytes,[13] and catalysts.[14] Consequently, preparation of a wide variety of ZrO_2 nanostructures, including thin films,[15] nanoparticles,[16] nanorods,[17] nanowires,[18] as well as nanotubes,[19] have been intensively and extensively studied. Among them, ZrO_2 nanorods, nanowires, and nanotubes were prepared through sol–gel and solid–gas multi-phase reactions with the help of diverse sacrificial templates, including AAO,[18] polyester track-etched membrane (PETE),[20] BN nanotubes,[21] and carbon fibers.[22] The fabrication of YSZ nanotubes[23] followed the same route and was achieved with an AAO assisted sol–gel process. As a result, sacrificial templates were necessary in the past for preparation of 1D nanostructures of ZrO_2 and YSZ. In this study, for the first time, ZrO_2 and YSZ nanorod arrays were fabricated via a non-catalytic, template-free MOCVD process in one-step.

For typical crystal growth, isotropic growth results in 0D products, whereas anisotropic growth is necessary to grow 1D nanostructures. To achieve anisotropic growth, there have been developed several techniques,[24] including induction growth of materials possessing anisotropic crystallographic structure, use of guiding catalysts (VLS), sacrificial templates, and capping reagents, anisotropic self-assembly of 0D nanostructures, and size reduction from 1D microstructures. The present work explores the possibility of phase-transition assisted 1D nanostructure growth. Anisotropic growth accompanied with phase transition in fact was demonstrated before with the formation of tetrapods. For tetrapod formation of II–VI semiconductors, such as CdS,[25] CdSe,[26] and CdTe,[27] phase transition from zinc blende core to wurtzite arms was observed. Zirconia possesses three major crystalline phases, monoclinic at low temperatures (<1200 °C) and transitions to tetragonal (1200–2370 °C) to cubic (>2370 °C) phases at increasing temperatures.[28] A tetragonal crystal lattice is created from stretching a cubic crystal lattice along one of the three lattice vectors, and it is thus anisotropic and a preferential growth habit may be established along the elongated direction, leading to 1D nanostructures. In fact, there have been demonstrated several examples of 1D nanostructure growth for materials possessing tetragonal crystalline phases, including Sn,[29] SnO_2,[30] and TiO_2.[31] In view of the above, a monoclinic to tetragonal phase transition may be stimulated in ZrO_2 preparation to achieve 1D growth of ZrO_2 nanostructures.

[a]Department of Chemical Engineering, National Tsing-Hua University, Hsinchu, Taiwan, 30013, R. O. C. E-mail: sylu@mx.nthu.edu.tw

[b]Department of Chemical Engineering and R&D Center for Membrane Technology, Chung Yuan Christian University, Chungli, Taiwan, 320, R. O. C. E-mail: yflin@cycu.edu.tw

[c]Department of Material Science and Engineering, National Chiao Tung University, Hsinchu, Taiwan, 30010, R. O. C

In this work, we present the first example of the monoclinic to tetragonal phase transition assisted 1D nanostructure formation. Well-aligned ZrO_2 nanorod arrays were fabricated *via* a non-catalytic, template-free MOCVD process using a single source precursor, $Zr(C_5H_7O_2)_4$, with the reaction temperature set at 1000 °C, a temperature close to the monoclinic-tetragonal phase transition of ZrO_2. With co-feeding of an yttria precursor, YCl_3, the same process produced YSZ nanorod arrays. These well-aligned and densely distributed ZrO_2 and YSZ nanorod arrays may serve as a better format than randomly distributed nanorods for fabrication of nano-devices. The proposed 1D growth concept can be readily extended to other nanomaterials possessing the monoclinic-tetragonal polymorphism, such as HfO_2.

Experimental

Preparation of ZrO_2 nanostructures and YSZ nanorod arrays

ZrO_2 nanostructures and YSZ nanorod arrays were prepared with a hot wall MOCVD process operated in a three-zone tube furnace with p-type Si(100) plates serving as the collection substrates. For preparation of the ZrO_2 nanostructures, $Zr(C_5H_7O_2)_4$ powders were fed into a precursor boat and heated to 160 °C to generate the precursor vapours. The furnace temperature was set at 550, 700, or 1000 °C and the system pressure was maintained at 30 Torr. Nitrogen and oxygen were introduced into the reactor both at a flow rate of 100 sccm to serve as the carrier and reactant gases, respectively. All depositions were run for 6 h, and the system was allowed to cool naturally in nitrogen atmosphere to room temperature for 2 h after the deposition. As for the preparation of the YSZ nanorod arrays, the same set up and processing conditions were used except that a second precursor, YCl_3 powders for the incorporation of yttria as a phase stabilizer for zirconia, was placed inside the furnace at a location 11 cm upstream from the center of the furnace, where the temperature was measured to be 825 °C with the furnace temperature set at 1000 °C.

Cooling procedures of as-grown ZrO_2 nanostructures

To investigate the cooling rate effect on the product phase, we conducted two more cooling procedures in addition to the natural cooling practice: slow and fast cooling. For the slow cooling procedure, a stepwise cooling pattern was used, with the system temperature in each cooling step decreased by 100 °C at a cooling rate of 1 °C min^{-1} and held at that temperature for 12 h. This stepwise cooling was performed from 1000 to 500 °C, and then the furnace was turned off and let cool naturally to room temperature for 1 h. The total cooling time of this procedure was about 61 h. As for the fast cooling procedure, we increased the flow rate of nitrogen gas from 100 to 1000 sccm to enhance the forced convective heat transfer to achieve faster cooling. The total cooling time of this procedure was about 1.5 h.

Characterizations

Thermal gravimetric (TG) analyses of the precursor were carried out with Seiko SSC 5000 instrument using a heating rate of 5 °C min^{-1}. The morphology and dimension of the as-grown samples were examined by a field emission scanning electron microscope (FESEM, Hitachi, S-4700). The crystallographic structures of the as-deposited nanostructures were studied with X-ray diffraction (XRD, MAC Science MXP18) and transmission electron microscope (TEM, JEOL JEM-2010, operated at 200 kV). The elemental analyses of individual ZrO_2 and YSZ nanorods were conducted with an energy dispersive spectrometer (EDS), an accessory of the TEM.

Results and discussion

The thermal decomposition behaviour of $Zr(C_5H_7O_2)_4$ was checked first with the TG analysis, from which one can set the reaction temperature accordingly. As shown in Fig. 1. the thermal decomposition of the precursor started at around 130 °C and a sharp drop in weight occurred at temperatures up to 200 °C. The sample weight levelled off at 550 °C to a remaining weight percent of 27. This final weight percentage of 27 agreed quite well with the molecular weight ratio of ZrO_2 to $Zr(C_5H_7O_2)_4$, 25%, implying formation of zirconia as the thermal decomposition product of the precursor. With this, we set the reaction temperature at least 550 °C to ensure formation of zirconia in the MOCVD process.

The surface morphologies of the as-deposited ZrO_2 nanostructures were first examined with FESEM. At the reaction temperature of 550 °C, the deposit appeared to be a layer of particle film of 500 nm thick, as shown in Fig. 2(a). With the reaction temperature increased to 700 °C, the product morphology, Fig. 2(b), became tree-like structures composed of nanoparticles. These tree-like structures, with a height of 500 nm and diameter of 50–100 nm, turned more one-dimensional in appearance as compared with that of the 550 °C case. With the reaction temperature further increased to 1000 °C, well-aligned, densely distributed ZrO_2 nanorods were found to grow on top of a thin buffer layer laid on the substrate surface, Fig. 2(c). The nanorods were 500 nm in height and 100 nm in diameter. Fig. 2(d) shows the corresponding XRD patterns of the as-grown ZrO_2 nanostructures at the three reaction temperatures. Also included in Fig. 2(d) are the reference patterns of the monoclinic (JCPDS # 88-2390) and tetragonal (JCPDS # 88-1007) phases of ZrO_2 crystals for comparison purposes. Evidently, only
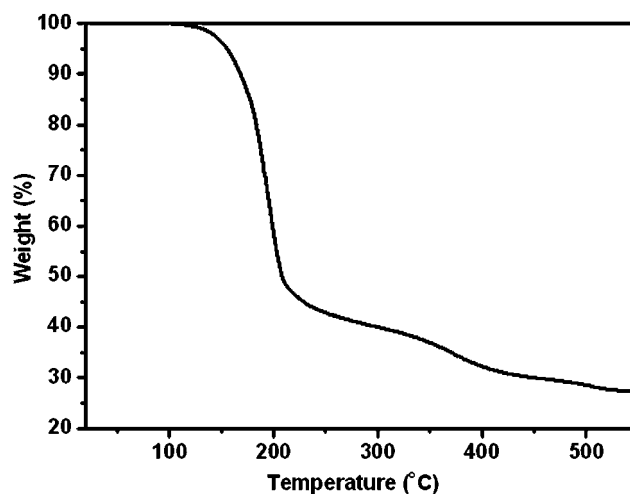

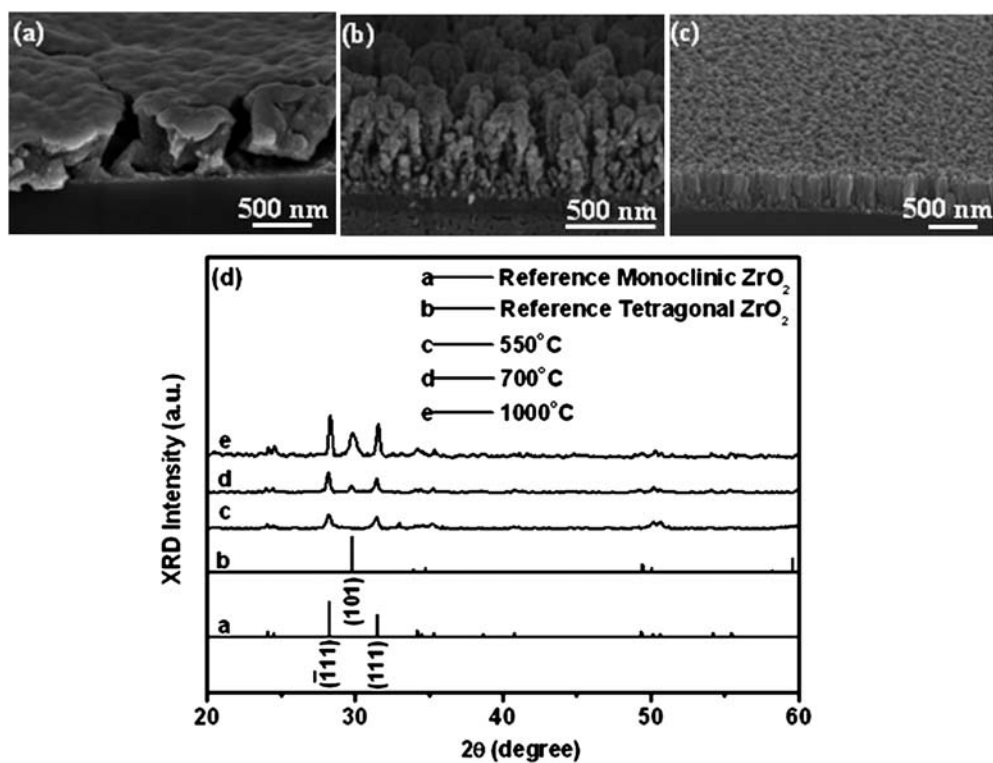**Fig. 1** TG analysis of the zirconia precursor, zirconium acetylacetonate.

Fig. 2 Tilt SEM images of ZrO_2 nanostructures prepared at reaction temperatures of (a) 550, (b) 700, and (c) 1000 °C. (d) XRD patterns of the as-grown ZrO_2 nanostructures.

monoclinic phase was present in the product of the 550 °C case. When the reaction temperature was increased to 700 °C, a minor amount of tetragonal phase appeared. The tetragonal phase became even more pronounced for the 1000 °C case, although the dominant phase was still monoclinic. The trend in the emergence of the tetragonal phase correlated well with the more one-dimensional morphology of the product.

To investigate whether or not phase transition did exist in the nanorod deposit, the detailed crystallographic structures of an individual ZrO_2 nanorod and the thin buffer layer released from the Si substrate, were further studied with HRTEM. Ultrasonic agitation was applied to a beaker of ethanol containing the sample to separate the buffer layer from the substrate and nanorods. Fig. 3(a) shows an HRTEM image of an individual ZrO_2 nanorod. The grain boundary between the tetragonal and monoclinic phases is evident, as indicated by a black dashed line, exhibiting the phase transition from monoclinic to tetragonal

phase along the axis of the ZrO_2 nanorod. The lattice-resolved image also shows lattice spacing of 0.3 and 0.25 nm, in good agreement with the d-spacing of the (101) and (002) planes of tetragonal ZrO_2. Furthermore, the lattice spacing of 0.5 nm was consistent with the d-spacing of the (100) planes of monoclinic ZrO_2. Fig. 3(b)–(d) are the fast Fourier transform (FFT) images taken at the three marked regions in Fig. 3(a). These FFT images further confirm the existence of pure tetragonal, mixed tetragonal and monoclinic, and pure monoclinic regions of the ZrO_2 nanorod. Fig. 3(e) displays the TEM-EDS spectrum of a single nanorod. The copper and carbon signals came from the hole-filled carbon film-supported copper grid used to hold the samples. The Zr and O signals were detected at an atomic Zr : O ratio of about 34 : 66, confirming the ZrO_2 composition. Fig. 4(a) shows a TEM image of the thin buffer layer, and
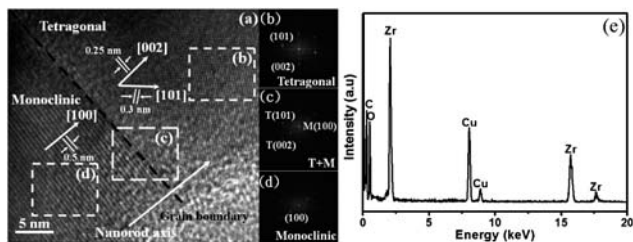

Fig. 3 (a) HRTEM image of a ZrO_2 nanorod prepared at 1000 °C, and (b)–(d) the corresponding FFT patterns of the marked regions in (a). (e) The TEM-EDS spectrum of the as-grown ZrO_2 nanorods.
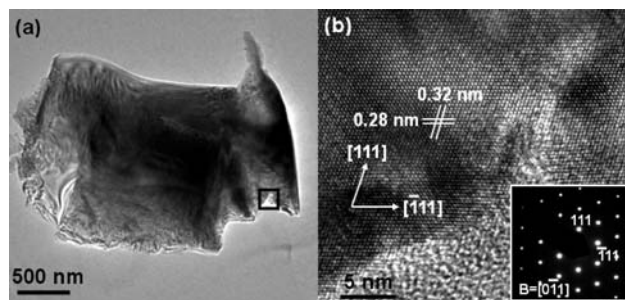

Fig. 4 (a) TEM image of the thin buffer layer obtained at 1000 °C. (b) HRTEM image of the marked region in (a). The inset is the corresponding SAED pattern of the thin buffer layer.

Fig. 4(b) is the HRTEM image of the marked region in Fig. 4(a). The lattice spacing was determined to be 0.32 and 0.28 nm, in good agreement with the d-spacing of the $(\bar{1}11)$ and (111) planes of monoclinic ZrO_2, respectively. The inset of Fig. 4(b) shows the corresponding selected area electron diffraction (SAED) pattern of the buffer layer. The zone axis of the SAED pattern was set in the $[0\bar{1}1]$ direction, and the resulting dot pattern suggested the single crystalline nature of the ZrO_2 buffer layer with the dots contributed by the reflections of the monoclinic ZrO_2. The results of Fig. 3 and 4 together suggest that a thin single crystalline buffer layer of monoclinic phase was formed first, with the nanorods later grown on top of it. Note that both the lattice constants $b = 5.21$ and $c = 5.15$ Å of monoclinic ZrO_2 match closely with the lattice constant $a = 5.43$ Å of Si, giving small lattice mismatches of 4–5%. This would favour the growth of a monoclinic ZrO_2 buffer layer on top of the Si substrate.

A phase transition from monoclinic to tetragonal phase occurred during the nanorod growth to further favor the continuing 1D growth of ZrO_2. Here, we performed a surface free energy density analysis for the different crystallographic planes of tetragonal ZrO_2 to show that the [002] is indeed a preferred growth direction for anisotropic growth of tetragonal ZrO_2. The crystallographic structure of tetragonal ZrO_2 is shown in Fig. 5(a). The surface free energy density of a specific crystallographic plane (hkl) can be expressed as $g_{hkl} = \dfrac{\sum_i \mu_i n_i}{A_{hkl}}$, where μ_i and n_i are the chemical potential and number of atoms of element i, respectively, present on the hkl plane, and A_{hkl} is the area of the hkl plane. There can be identified 4 different crystallographic planes, (002), {010}, {011} and (110), for the tetragonal phase of ZrO_2 as illustrated in Fig. 5(b)–(e). The surface free energy densities of these planes can be calculated as follows.

$$g_{(002)} = \frac{5 \times \mu_{Zr}}{a^2} = \frac{4 \times \mu_{Zr} + \mu_{Zr}}{3.64^2} \tag{1}$$

$$g_{\{010\}} = \frac{5 \times \mu_{Zr}}{a \times c} = \frac{4 \times \mu_{Zr} + \mu_{Zr}}{3.64 \times 5.27} \tag{2}$$

$$g_{\{011\}} = \frac{6 \times \mu_{Zr} + 4 \times \mu_O}{a \times \sqrt{a^2 + c^2}} = \frac{6 \times \mu_{Zr} + 4 \times \mu_O}{3.64 \times 6.40} \tag{3}$$

$$g_{(110)} = \frac{6 \times \mu_{Zr} + 4 \times \mu_O}{\sqrt{2}a \times c} = \frac{6 \times \mu_{Zr} + 4 \times \mu_O}{5.15 \times 5.27} \tag{4}$$

Here, a and c are the lattice constants of tetragonal ZrO_2, having the values of 3.64 and 5.27 Å, respectively. The unit of g is eV Å^{-2}. To compare the magnitude of these surface free energy densities, one needs more information about μ_{Zr} and μ_O. The formation energy of ZrO_2 is -12.1 eV,[32] which gives the following relations.

$$\mu_{Zr} + 2 \times \mu_O = -12.1 \tag{5}$$

$$\mu_{Zr} \leq 0, \; \mu_O \leq 0 \tag{6}$$

Eqn (5) and (6) lead to

$$-12.1 \leq \mu_{Zr} \leq 0 \tag{7}$$

Taking eqn (5) into consideration, eqn (3) and (4) then become

$$g_{\{011\}} = \frac{4\mu_{Zr} - 24.2}{3.64 \times 6.40} \tag{8}$$

$$g_{(110)} = \frac{4\mu_{Zr} - 24.2}{5.15 \times 5.27} \tag{9}$$

From eqn (1), (2), (7), (8), and (9), one can conclude that $g_{(002)} > g_{\{010\}} > g_{\{011\}} > g_{(110)}$ in magnitude. Evidently, the (002) plane possesses the highest surface free energy density and is thus thermodynamically the least stable, favouring anisotropic growth of tetragonal ZrO_2 under suitable growth conditions. The growth along the [002] direction creates the more stable facets of {010}. The above analysis also explains why the growth direction is [002] for the tetragonal ZrO_2 nanorods as observed in Fig. 3(a).

We proceeded further to prepare YSZ nanorod arrays by co-feeding the precursor for the phase stabilizer, YCl_3, to dope in situ the zirconia nanorods during their growth. Fig. 6(a) shows a tilt SEM image of the as-grown, densely distributed nanorod arrays of YSZ. The YSZ nanorods had diameters of 50–100 nm and lengths of about 250 nm. As expected, with yttria doping, only one ZrO_2-related crystalline phase was observed in the XRD pattern of the YSZ nanorod array. Fig. 6(b) also shows the reference pattern of the cubic $Zr_{0.8}Y_{0.2}O_{1.9}$ (JCPDS # 82-1246) for comparison purposes. Both patterns were in good agreement with each other, indicating that the as-grown nanorods possessed a cubic crystalline structure of YSZ, containing a 10 mol% of Y_2O_3. Nevertheless, a careful examination of the XRD pattern of the YSZ nanorods revealed several minor peaks attributable to YCl_3, implying the presence of unreacted YCl_3 in the product. In addition, the grain size of the as-grown YSZ was estimated with the Scherrer formula to be about 20 nm. This size was smaller
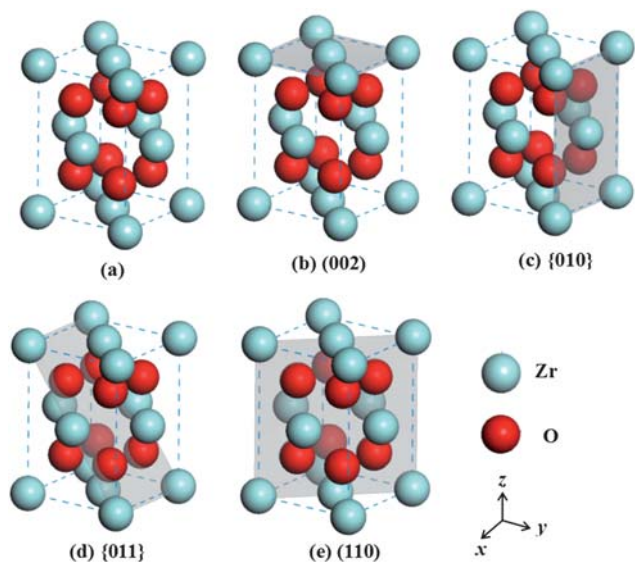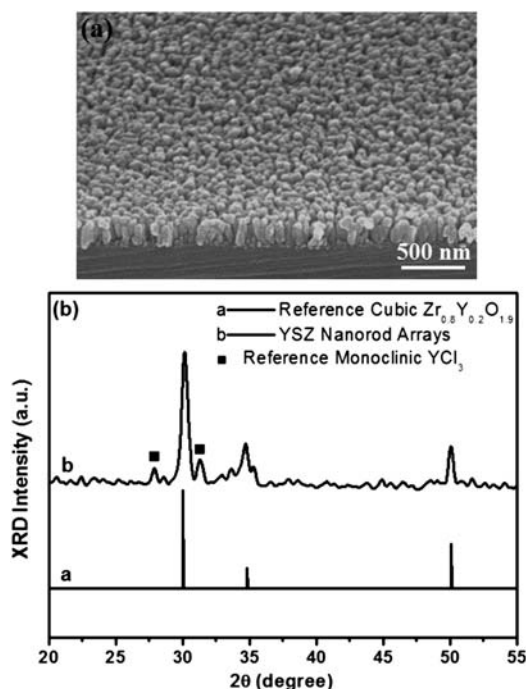
Fig. 5 (a) Crystallographic structure of tetragonal ZrO_2. (b)–(d) The (002), {010}, {011}, and (110) planes of tetragonal ZrO_2.

Fig. 6 (a) SEM image and (b) XRD pattern of the YSZ nanorod arrays.

than the diameter of the YSZ nanorod (50–100 nm), indicating the polycrystalline nature of the YSZ nanorods.

Fig. 7(a) shows the HRTEM image of a single YSZ nanorod. Evidently, the nanorod was polycrystalline, and the grain boundaries existing in the nanorod were evident, as indicated by the white dashed lines. The grain size estimated from the image agreed well with that approximated by the Scherrer equation. The lattice spacing was determined to be 0.3 nm, in good agreement with the d-spacing of the (111) planes of cubic $Zr_{0.8}Y_{0.2}O_{1.9}$. The zone axis of the SAED pattern was set in the $[1\bar{1}0]$ direction, and the resulting ring pattern suggested the polycrystalline nature of the YSZ nanorods with the rings contributed by the reflections of the cubic $Zr_{0.8}Y_{0.2}O_{1.9}$, consistent with the corresponding XRD results. Fig. 7(c) displays the TEM-EDS spectrum of a single YSZ nanorod. The copper and carbon signals again came from the sample holder. The Zr and Y
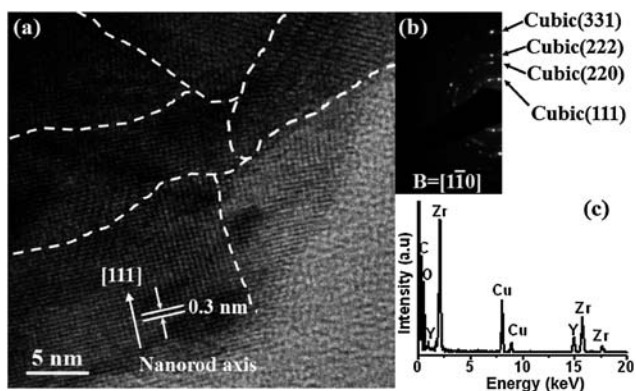

Fig. 7 (a) HRTEM image, (b) SAED patterns, and (c) TEM-EDS spectrum of the as-grown YSZ nanorods.
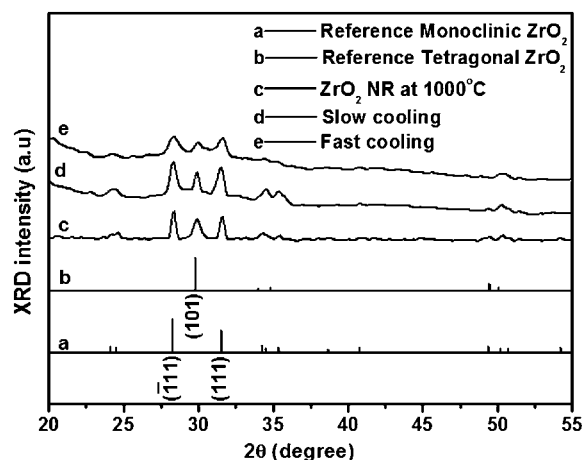

Fig. 8 XRD patterns of as-grown YSZ nanorod arrays prepared at 1000 °C with three different cooling procedures.

signals were detected in an atomic Zr : Y ratio of about 4 : 1, corresponding to a 10 mol% doping of Y_2O_3 in the YSZ nanorod.

For the growth of the YSZ nanorods, we propose that the ZrO_2 nanorods formed first, followed by the *in situ* Y-doping in the ZrO_2 nanorods to form the YSZ nanorods. Since the YSZ is stable at the cubic phase, there would be involved phase transition from monoclinic or tetragonal to cubic.

Finally, we investigated the possible cooling rate effect on the product phase. Recall that zirconia possesses three major crystalline phases, depending on temperature. When the product is prepared at high temperatures, the cooling from high temperatures to room temperature may initiate phase transition. We compared zirconia deposits collected from depositions with three different cooling procedures: slow, natural, and fast. The resulting XRD patterns were compared in Fig. 8. Evidently, the three patterns were quite similar to one another. To make the comparison more quantitative, we calculated the peak intensity ratios of tetragonal (101) to monoclinic ($\bar{1}$11) to see if the relative amount of the two phases changed with cooling practices. The three ratios all fell in the neighbourhood of 65% regardless of the cooling practice. This outcome indicates that for the present work the crystalline phase of the product was determined at the growth stage and was irrelevant to the post-growth cooling.

Conclusion

In conclusion, a non-catalytic, template-free MOCVD process was developed to produce well-aligned, densely distributed ZrO_2 and YSZ nanorods. The anisotropic growth of zirconia, necessary for the formation of nanorod arrays, was found to be assisted by a monoclinic to tetragonal phase transition that occurred during the nanorod growth. Based on this process, an *in situ* doping of the zirconia nanorod array with yttria led to the formation of YSZ nanorod arrays. From the cooling rate study, one concludes that the phase of the nanorod product was determined at the growth stage of the nanorods. This is advantageous for control of the product phases. The present method of phase-transition assisted 1D growth may be extended to other

material systems possessing the monoclinic-tetragonal polymorphism.

Acknowledgements

References

1 (a) Y.-F. Lin, Y.-J. Hsu, S.-Y. Lu and S.-C. Kung, *Chem. Commun.*, 2006, 2391; (b) Y.-F. Lin, Y.-J. Hsu, S.-Y. Lu, K.-T. Chen and T.-Y. Tseng, *J. Phys. Chem. C*, 2007, **111**, 13418.
2 (a) X. Zhang, A. Gu, G. Wang, Y. Wei, W. Wang, H. Wu and B. Fang, *CrystEngComm*, 2010, **12**, 1120; (b) Y.-F. Lin, Y.-J. Hsu, W.-Y. Cheng and S.-Y. Lu, *ChemPhysChem*, 2009, **10**, 711.
3 Y.-F. Lin, J. Song, Y. Ding, S.-Y. Lu and Z. L. Wang, *Appl. Phys. Lett.*, 2008, **92**, 022105.
4 Z. L. Wang and J. Song, *Science*, 2006, **312**, 242.
5 D. Routkevitch, T. Bigioni, M. Moskovits and J. M. Xu, *J. Phys. Chem.*, 1996, **100**, 14037.
6 (a) X. Wang, J. Song, P. Li, J. H. Ryou, R. D. Dupuis, C. J. Summers and Z. L. Wang, *J. Am. Chem. Soc.*, 2005, **127**, 7920; (b) M. J. Zheng, L. D. Zhang, G. H. Li and W. Z. Shen, *Chem. Phys. Lett.*, 2002, **363**, 123.
7 Q. Zhang, Y. Li, D. Xu and Z. Gu, *J. Mater. Sci. Lett.*, 2001, **20**, 925.
8 T. Kuykendall, P. J. Pauzauskie, Y. Zhang, J. Goldberger, D. Sirbuly, J. Denlinger and P. Yang, *Nat. Mater.*, 2004, **3**, 524.
9 L. Li, Y. Yang, X. Huang, G. Li and L. Zhang, *J. Phys. Chem. B*, 2005, **109**, 12394.
10 C. Jin, G. Zhang, T. Qian, X. Li and Z. Yao, *J. Phys. Chem. B*, 2005, **109**, 1430.
11 Y.-F. Lin, Y.-J. Hsu, S.-Y. Lu and W.-S. Chiang, *Nanotechnology*, 2006, **17**, 4773.
12 N. Rajabbeigi, B. Elyassi, A. A. Khodadadi, S. Mohajerzadeh, Y. Mortazavi and M. Sahimi, *Sens. Actuators, B*, 2005, **108**, 341.
13 M. Mamak, N. Coombs and G. Ozin, *J. Am. Chem. Soc.*, 2000, **122**, 8932.
14 Y. Li, D. He, Z. Cheng, C. Su, J. Li and Q. Zhu, *J. Mol. Catal. A: Chem.*, 2001, **175**, 267.
15 F. C. M. Woudenberg, W. F. C. Sager, J. E. Elshof and H. Verweij, *J. Am. Ceram. Soc.*, 2004, **87**, 1430.
16 N. N. Khimich, O. V. Semashko, E. N. Khimich and M. G. Voronkov, *Russ. J. Appl. Chem.*, 2006, **79**, 351.
17 Y. Liu, C. Zheng, W. Wang, Y. Zhan and G. H. Wang, *J. Am. Ceram. Soc.*, 2002, **85**, 3120.
18 H. Xu, D.-H. Qin, Z. Yang and H.-L. Li, *Mater. Chem. Phys.*, 2003, **80**, 524.
19 H. Tsuchuya, J. M. Macak, L. Taverira and P. Schmuki, *Chem. Phys. Lett.*, 2005, **410**, 188.
20 H. Chen, Y. A. Elabd and G. R. Palmese, *J. Mater. Chem.*, 2007, **17**, 1593.
21 Z. Q. Shen, L. L. He, E. D. Wu, Y. Y. Fan, J. F. He, H. M. Cheng, D. X. Li and H. Q. Ye, *J. Mater. Res.*, 2002, **17**, 2761.
22 H. Ogihara, M. Sadakane, Y. Nodasaka and W. Ueda, *Chem. Mater.*, 2006, **18**, 4981.
23 X. Meng, X. Tan, B. Meng, N. Yang and Z.-F. Ma, *Mater. Chem. Phys.*, 2008, **111**, 275.
24 Y. Xia, P. Yang, Y. Sun, Y. Wu, B. Mayers, B. Gates, Y. Yin, F. Kim and H. Yan, *Adv. Mater.*, 2003, **15**, 353.
25 S.-M. Lee, S.-N. Cho and J. Cheon, *Adv. Mater.*, 2003, **15**, 441.
26 (a) A. Fiore, R. Mastria, M. G. Lupo, G. Lanzani, C. Giannini, E. Carlino, G. Morello, M. D. Giorgi, Y. Li, R. Cingolani and L. Manna, *J. Am. Chem. Soc.*, 2009, **131**, 2274; (b) Q. Pang, L. Zhao, Y. Cai, D. P. Nguyen, N. Regnault, N. Wang, S. Yang, W. Ge, R. Ferreira, G. Bastard and J. Wang, *Chem. Mater.*, 2005, **17**, 5263.
27 J. W. Cho, H. S. Kim, Y. J. Kim, S. Y. Jan and J. Park, *Chem. Mater.*, 2008, **20**, 5600.
28 H. G. Scott, *J. Mater. Sci.*, 1975, **10**, 1527.
29 Y.-J. Hsu, S.-Y. Lu and Y.-F. Lin, *Small*, 2006, **2**, 268.
30 (a) J. Hu, Z. Chen, R. Zou and Y. Sun, *CrystEngComm*, 2010, **12**, 89; (b) R. Yang and Z. L. Wang, *J. Am. Chem. Soc.*, 2006, **128**, 1466.
31 (a) A. K. Sinha, S. Jana, S. Pande, S. Sarkar, M. Pradhan, M. Basu, S. Saha, A. Pal and T. Pal, *CrystEngComm*, 2009, **11**, 1210; (b) J.-J. Wu and C.-C. Yu, *J. Phys. Chem. B*, 2004, **108**, 3377.
32 J. M. Pruneda and E. Artacho, *Phys. Rev. B: Condens. Matter Mater. Phys.*, 2005, **71**, 094113.